Applied and Computational Mathematics
2026, Vol. 15, No. 6, pp. 244–256
https://doi.org/10.11648/j.acm.20261506.13

Research Article

Mathematical Model of Sickle Cell Blood Flow with Morphological Effect Under an Inclined Variable Magnetic Field

Maurine Aloo *, Mathew Ngugi Kinyanjui, Edward Richard Onyango

Department of Pure and Applied Mathematics, Jomo Kenyatta University of Agriculture and Technology, Juja, Kenya

Abstract

Sickle cell anaemia transforms flexible biconcave erythrocytes into rigid, adhesive, sickle-shaped cells that raise the resistance to blood flow and promote vaso-occlusion. This study develops a mathematical model of unsteady, pulsatile blood flow in a sickle cell anaemia patient through a rigid cylindrical vessel subjected to a magnetic field inclined at an angle to the vessel axis, coupled with heat transfer, the transport of a reacting chemical species and magnetic induction. The rigidity of sickled cells is represented by a Darcy-type morphological resistance parameter Mo, and the energy equation includes Joule and morphological heating together with thermal radiation. The continuity, momentum, energy, concentration and induction equations are non-dimensionalised and solved with an implicit Crank–Nicolson finite difference scheme and the Thomas algorithm in MATLAB, and the solver is verified against exact Bessel-function solutions, with which the computed profiles agree to within 5×10^{-4}. Velocity, temperature, concentration and induced magnetic field profiles, together with the skin friction, Nusselt and Sherwood numbers, are reported for every parameter of the model. Increasing the Hartmann number from 0 to 6 lowers the peak velocity by 44% and the skin friction by 28%, while increasing Mo from 0 to 8 lowers them by 38% and 24%. The inclination of the field is itself an effective control variable: rotating the field from parallel to perpendicular to the flow reduces the peak velocity by 26%. The Hartmann number, the inclination angle α and Mo act on the flow only through the single combination $m^2 = Ha^2 \sin^2 \alpha + Mo$, so that a magnetic field and a degree of sickling with equal m^2 produce identical flows. Thermal and solutal buoyancy accelerate the flow, thermal radiation cools the core and steepens the wall heat flux, and stronger chemical reaction or weaker mass diffusion depletes the species in the core. The induced axial magnetic field grows with the magnetic Reynolds number. The results quantify how sickle cell morphology and an inclined magnetic field jointly control haemodynamics in sickle cell anaemia.

Keywords

Sickle Cell Anaemia, Morphological Effect, Inclined Magnetic Field, Magnetohydrodynamics, Pulsatile Blood Flow, Heat and Mass Transfer, Crank–Nicolson Method

1. Introduction

Sickle cell anaemia (SCA) is an inherited disorder caused by a single substitution in the β-globin (HBB) gene. The resulting haemoglobin S polymerises on deoxygenation and distorts the normally round, biconcave red blood cell (RBC) into a rigid, sticky, crescent or sickle shape [1, 2]. Healthy erythrocytes lack a nucleus, which makes room for haemoglobin and allows the cell to deform and squeeze through narrow capillaries; sickled cells lose this deformability, become lodged in small vessels,

*Correspondence: Maurine Aloo (maurinealoo023@gmail.com)

Received: 28 September 2026; **Accepted:** 13 October 2026; **Published:** 16 November 2026

Copyright: © The Author(s), 2026. Published by Science Publishing Group. This is an **Open Access** article, distributed under the terms of the Creative Commons Attribution 4.0 License (http://creativecommons.org/licenses/by/4.0/), which permits unrestricted use, distribution and reproduction in any medium, provided the original work is properly cited.

obstruct flow and die early, producing chronic anaemia, pain crises, acute chest syndrome and stroke [2, 3]. The Global Burden of Disease Study estimated that 7.74 million people were living with sickle cell disease in 2021, with about 515 000 affected births that year and the heaviest burden in sub-Saharan Africa [4]. Only a few disease-modifying drugs, including hydroxyurea, L-glutamine and crizanlizumab, are approved, so there is continuing interest in physical means of understanding and influencing sickle cell haemodynamics.

At the continuum level, sickling is first of all a rheological change. Blood from patients with SCA shows abnormal viscosity even when oxygenated, and patients with poorly deformable cells experience more frequent vaso-occlusive events [5, 6]. Chaturvedi and Shah [7] modelled a single sickle cell in a capillary with slip at the wall and found that cell distortion thickens the plasma layer, while hard, adhesive cells reduce the forward velocity and favour occlusion. Cell-resolved simulations show that healthy cells move faster than sickle cells through a stenosis, that sickle cells raise the apparent viscosity and flow resistance [8], that rigid cells deform less than normal cells under the same load [9, 10], and that cell deformation and aggregation depend strongly on confinement, curvature and bifurcations [11–14]. Reviews of cell-scale blood flow simulation [15] and multiscale methods bridging mesoscopic and continuum descriptions [16] emphasise the cost of such models. At the vessel scale, Keller *et al.* [17] showed that a standard blood viscosity model overpredicted peak wall shear stress in the circle of Willis of SCA patients by 55% in steady and 49% in pulsatile flow, and Sawyer *et al.* [18] used computational fluid dynamics (CFD) to relate transfusion to cerebral wall shear stress. Tekleab and Harris [19] used a Crank–Nicolson scheme to model plasma flow with oxygen transport and membrane deformation.

Blood is a weak electrical conductor, and haemoglobin contains iron, so a magnetic field interacts with flowing blood through a retarding Lorentz force [20–22]. Atalla *et al.* [23] modelled the magnetic disturbance created by pulsatile blood in a static field, and a large body of mathematical work has combined magnetohydrodynamics (MHD) with heat transfer, thermal radiation and chemical reaction in arterial flow [24–26]. In these models a stronger constant magnetic field consistently decelerates the flow [26], and Sankar *et al.* [27] found that high-intensity constant fields reduce oxygen transfer to tissue. Closest to the present work, Ekakitie *et al.* [28] introduced a morphological effect into an MHD model of blood flow in an SCA patient under a constant magnetic field and found that increasing the field decreases the flow, increases the wall shear stress and decreases the volumetric flow rate.

Two aspects of this problem have received little attention. First, previous studies treat the applied field as constant and transverse, so the *orientation* of the field relative to the flow, as distinct from the inclination of the artery, has not been examined as a control variable. Second, the morphological effect has not been examined together with an inclined field, induced magnetic field, heat and mass transfer in one pulsatile model. The aim of this study is therefore to model the flow of sickle cell blood under an inclined, variable magnetic field. The specific objectives are to (i) develop a mathematical model for blood flow in an SCA patient that accounts for cell morphology and an inclined magnetic field, (ii) determine the velocity, temperature, concentration and induced magnetic field profiles, and (iii) determine the effects of the flow parameters on these variables and on the wall transfer rates. In addition to the parametric study, we show that the field strength, its inclination and the morphological parameter combine into a single resistance $m^2 = Ha^2 \sin^2 \alpha + Mo$, and we verify the numerical scheme against exact solutions.

2. Mathematical Formulation

2.1. Physical Model and Assumptions

We consider the flow of blood containing both normal and sickled erythrocytes through a straight, rigid, circular vessel of radius R, in cylindrical coordinates (r, θ, z) with z along the vessel axis (Figure 1). A magnetic field of strength B_0 is applied at an angle α to the vessel axis, so that its components are $B_0 \sin \alpha$ in the radial direction and $B_0 \cos \alpha$ along the axis. The flow is driven by a pulsatile pressure gradient with a steady and an oscillatory part. The wall is held at a fixed temperature and species concentration, and the species is consumed in the lumen by a first-order chemical reaction. The assumptions are: (i) the fluid is incompressible, electrically conducting and Newtonian, with the rigidity of sickled cells represented by an additional linear resistance; (ii) the flow is laminar, unsteady, axisymmetric and purely axial, $\mathbf{u} = u(r, t)\, \mathbf{e}_z$; (iii) the no-slip condition holds at the wall; (iv) the Boussinesq approximation applies to thermal and solutal buoyancy; and (v) the imposed electric field is negligible.

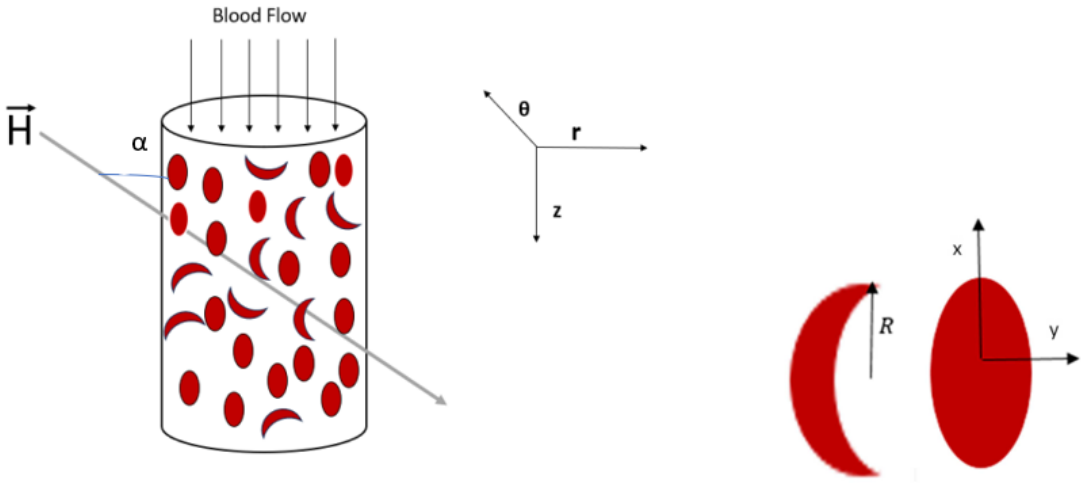


Figure 1. Geometry of the flow problem: blood containing normal and sickled red blood cells flows along the z-axis of a cylindrical vessel under a magnetic field $\vec{H}$ inclined at angle α to the vessel axis. Right: a sickled cell of characteristic radius R and a normal erythrocyte.

2.2. Governing Equations

Since the flow is incompressible and purely axial, the continuity equation reduces to $\partial u/\partial z = 0$, so that $u = u(r,t)$. The total magnetic field is the sum of the applied and induced fields,

$$\mathbf{B} = (B_0 \sin\alpha + B_r)\,\mathbf{e}_r + (B_0 \cos\alpha + B_z)\,\mathbf{e}_z, \tag{1}$$

with $B_\theta = 0$. With Ohm's law $\mathbf{J} = \sigma(\mathbf{E} + \mathbf{u}\times\mathbf{B})$ and $\mathbf{E} \approx 0$, the only current is $J_\theta = \sigma u B_r^{\mathrm{tot}}$ and the axial Lorentz force is

$$(\mathbf{J}\times\mathbf{B})_z = -\sigma u\,(B_0 \sin\alpha + B_r)^2. \tag{2}$$

The field component parallel to the flow exerts no force. The radial component of the Lorentz force is balanced by a radial pressure gradient and does not affect the axial motion [29].

Sickled cells cannot align and deform with the flow, and they mechanically obstruct the lumen. Following the approach used for abnormal blood rheology and particulate suspensions, this is represented by a Darcy-type resistance $-\mu_m u$ in the momentum equation, where the morphological resistance coefficient μ_m increases with the fraction and rigidity of sickled cells [28, 30]. The same term produces a heating $\mu_m u^2$ in the energy equation. The axial momentum, energy, concentration and induction equations are then

$$\rho\frac{\partial u}{\partial t} = -\frac{\partial p}{\partial z} + \mu\nabla_r^2 u + \rho g\beta_T(T-T_0) + \rho g\beta_C(C-C_0) - \sigma(B_0\sin\alpha + B_r)^2 u - \mu_m u, \tag{3}$$

$$\rho c_p\frac{\partial T}{\partial t} = k\nabla_r^2 T - \frac{\partial q_r}{\partial r} + \sigma(B_0\sin\alpha + B_r)^2 u^2 + \mu_m u^2, \tag{4}$$

$$\frac{\partial C}{\partial t} = D\nabla_r^2 C - k_c C, \tag{5}$$

$$\frac{\partial B_r}{\partial t} = \eta\left(\nabla_r^2 B_r - \frac{B_r}{r^2}\right), \tag{6}$$

$$\frac{\partial B_z}{\partial t} = \frac{1}{r}\frac{\partial}{\partial r}\left(r\,u\,B_r^{\mathrm{tot}}\right) + \eta\,\nabla_r^2 B_z, \tag{7}$$

where $\nabla_r^2 = \partial^2/\partial r^2 + r^{-1}\partial/\partial r$, $B_r^{\mathrm{tot}} = B_0\sin\alpha + B_r$, ρ is the density, μ the viscosity, β_T and β_C the thermal and solutal expansion coefficients, c_p the specific heat, k the thermal conductivity, D the mass diffusivity, k_c the reaction rate constant and $\eta = 1/(\mu_0\sigma)$ the magnetic diffusivity. Radiation is described by the optically thin approximation, $\partial q_r/\partial r = 4\kappa_a^2(T-T_0)$, with κ_a the mean absorption coefficient [31]. Equations (6, 7) follow from the induction equation $\partial\mathbf{B}/\partial t = \nabla\times(\mathbf{u}\times\mathbf{B}) + \eta\nabla^2\mathbf{B}$ for a purely axial flow independent of z.

The initial and boundary conditions are

$$\begin{aligned} &u = 0,\ T = T_0,\ C = C_0,\ B_r = B_z = 0 && \text{at } t = 0,\\ &\partial_r u = \partial_r T = \partial_r C = 0 && \text{at } r = 0,\\ &u = 0,\ T = T_w,\ C = C_w,\ B_r = B_z = 0 && \text{at } r = R. \end{aligned} \tag{8}$$

2.3. Non-dimensionalisation

With velocity scale U, the dimensionless variables

$$r^* = \frac{r}{R},\quad t^* = \frac{tU}{R},\quad u^* = \frac{u}{U},\quad p^* = \frac{p}{\rho U^2},\quad \Theta = \frac{T - T_0}{T_w - T_0},$$
$$c = \frac{C - C_0}{C_w - C_0},\quad b_r^* = \frac{B_r}{B_0},\quad b_z^* = \frac{B_z}{B_0} \tag{9}$$

are introduced. Since $B_r \ll B_0$, the total transverse field is $b_r = \sin\alpha + b_r^* \approx \sin\alpha$. Dropping asterisks, the governing equations become

$$\frac{\partial u}{\partial t} = \frac{P_s + P_p\cos\omega t}{a\,Re} + \frac{1}{Re}\nabla_r^2 u + \frac{Gr}{Re^2}\Theta + \frac{Gc}{Re^2}c - \frac{Ha^2\sin^2\alpha + Mo}{Re}\,u, \tag{10}$$

$$\frac{\partial \Theta}{\partial t} = \frac{1}{Re\,Pr}\left(\nabla_r^2\Theta - 2Rd\,\Theta\right) + Ec\,\frac{Ha^2\sin^2\alpha + Mo}{Re}\,u^2, \tag{11}$$

$$\frac{\partial c}{\partial t} = \frac{1}{Re\,Sc}\nabla_r^2 c - 2Da\,c, \tag{12}$$

$$\frac{\partial b_r^*}{\partial t} = \frac{1}{Rm}\left(\nabla_r^2 b_r^* - \frac{b_r^*}{r^2}\right), \tag{13}$$

$$\frac{\partial b_z}{\partial t} = \frac{\sin\alpha}{r}\frac{\partial}{\partial r}(ru) + \frac{1}{Rm}\frac{\partial^2 b_z}{\partial r^2}, \tag{14}$$

subject to $u = 0$, $\Theta = c = 1$ and $b_r^* = b_z = 0$ at $r = 1$, symmetry at $r = 0$ and zero initial data. The steady and pulsatile pressure amplitudes P_s and P_p, the frequency ω and the constant a define the prescribed pressure gradient. The radial diffusion of b_z in Eq. (14) is represented by its second-derivative term, as in the computations reported here. Viscous dissipation, $(Ec/Re)(\partial u/\partial r)^2$, is not included in the computations; the thermal source in Eq. (11) is the combined Joule and morphological heating. The dimensionless groups are

$$Re = \frac{\rho U R}{\mu},\quad Ha = B_0 R\sqrt{\frac{\sigma}{\mu}},\quad Mo = \frac{\mu_m R^2}{\mu},$$
$$Gr = \frac{g\beta_T(T_w - T_0)R^3}{\nu^2},\quad Gc = \frac{g\beta_C(C_w - C_0)R^3}{\nu^2},$$
$$Pr = \frac{\mu c_p}{k},\quad Rd = \frac{2\kappa_a^2 R^2}{k},\quad Ec = \frac{U^2}{c_p(T_w - T_0)},$$
$$Sc = \frac{\nu}{D},\quad Da = \frac{k_c R}{2U},\quad Rm = \mu_0\sigma U R, \tag{15}$$

namely the Reynolds, Hartmann, morphological, thermal and solutal Grashof, Prandtl, radiation, Eckert, Schmidt, Damköhler and magnetic Reynolds numbers, with $\nu = \mu/\rho$. The base values used in this study are listed in Table 1. Setting $Mo = 0$ recovers normal erythrocyte morphology; increasing Mo represents increasingly severe sickling.

Table 1. Parameters of the model: base values and ranges used in the parametric study.

Parameter	Base	Range
Reynolds number Re	10	5–40
Hartmann number Ha	2	0–6
Field inclination α	30°	0–90°
Morphological parameter Mo	0	0–8
Thermal Grashof number Gr	2	0–8
Solutal Grashof number Gc	3	0–9
Prandtl number Pr	0.71	0.71–7
Eckert number Ec	0.02	0.02–0.4
Radiation parameter Rd	0.5	0–2
Schmidt number Sc	1	0.22–2
Damköhler number Da	1	0–2
Magnetic Reynolds number Rm	5	1–20
Pressure amplitudes P_s, P_p	2, 4	–
Frequency ω, constant a	1, 1.1824	–

2.4. Magneto-Morphological Resistance

In Eqs. (10) and (11), the Hartmann number, the field inclination and the morphological parameter appear only through the combination

$$m^2 = Ha^2\sin^2\alpha + Mo, \tag{16}$$

and they do not appear in Eq. (12) or in the boundary conditions. Because the solution of the system is unique, any two parameter sets with the same m^2 give identical velocity, temperature and concentration fields. A field of strength Ha at inclination α is therefore hydrodynamically equivalent to a degree of sickling $Mo = Ha^2\sin^2\alpha$. Since both contributions are non-negative, the static field considered here adds to, rather than offsets, the resistance due to sickled cells. In the same way, the periodic concentration field depends on Re, Sc and Da only through the Thiele modulus $\Phi = \sqrt{2\,Re\,Sc\,Da}$.

3. Numerical Method and Verification

3.1. Crank–Nicolson Scheme

Equations (10)–(14) are discretised on a uniform radial grid $r_i = i\Delta r$, $i = 0, \ldots, N-1$, using second-order central differences in space and the implicit Crank–Nicolson method in time

[32]. For the momentum equation this gives, at interior nodes,

$$-(\gamma-\zeta_i)u_{i-1}^{n+1}+\Big(1+2\gamma+\tfrac{\Delta t\,m^2}{2Re}\Big)u_i^{n+1}-(\gamma+\zeta_i)u_{i+1}^{n+1}$$
$$=(\gamma-\zeta_i)u_{i-1}^{n}+\Big(1-2\gamma-\tfrac{\Delta t\,m^2}{2Re}\Big)u_i^{n}+(\gamma+\zeta_i)u_{i+1}^{n}$$
$$+\Delta t\Big[\bar F+\frac{Gr}{Re^2}\Theta_i^n+\frac{Gc}{Re^2}c_i^n\Big], \tag{17}$$

with $\gamma=\Delta t/(2Re\,\Delta r^2)$, $\zeta_i=\Delta t/(4Re\,r_i\Delta r)$ and $\bar F$ the pressure forcing averaged over the time step. The energy, concentration and induction equations are discretised in the same way. At the axis, symmetry is imposed through the ghost value $f_{-1}=f_1$, so that $\nabla_r^2 f\to 4(f_1-f_0)/\Delta r^2$. Each time step requires the solution of five tridiagonal systems, which is performed with the Thomas algorithm [33]. The computations use $N=41$ ($\Delta r=0.025$) and $\Delta t=0.01$, starting from rest, and are advanced over four periods of the pressure forcing ($t=8\pi$); fifteen periods are used for the induced-field sweep, which converges more slowly at large Rm. Profiles are reported at the phase of peak pressure forcing, $\cos\omega t=1$. The skin friction, Nusselt and Sherwood numbers are evaluated from the wall gradients at $r=1$,

$$C_f=-\frac{\partial u}{\partial r}\Big|_1,\quad Nu=-\frac{\partial\Theta}{\partial r}\Big|_1,\quad Sh=-\frac{\partial c}{\partial r}\Big|_1, \tag{18}$$

approximated by the two-point difference $-(f_{N-1}-f_{N-2})/\Delta r$. With these definitions, $Nu<0$ and $Sh<0$ when heat and species pass from the wall into the blood.

3.2. Verification Against Exact Solutions

For $Ec=0$ the system (10)–(12) is linear and has an exact time-periodic solution. With I_0 and I_1 the modified Bessel functions of the first kind [34], $\lambda^2=2Rd$, $\Phi^2=2Re\,Sc\,Da$ and $k^2=m^2+\mathrm{i}\,\omega Re$,

$$\Theta=\frac{I_0(\lambda r)}{I_0(\lambda)},\qquad c=\frac{I_0(\Phi r)}{I_0(\Phi)}, \tag{19}$$

$$u=\frac{P_s}{a\,m^2}\Big[1-\frac{I_0(mr)}{I_0(m)}\Big]+u_b$$
$$+\mathcal{R}\Big\{\frac{P_p}{a\,k^2}\Big[1-\frac{I_0(kr)}{I_0(k)}\Big]e^{\mathrm{i}\omega t}\Big\}, \tag{20}$$

where $\mathcal{R}\{\cdot\}$ denotes the real part and u_b is the buoyancy-driven part, obtained from $(\nabla_r^2-m^2)u_b=-(Gr\,\Theta+Gc\,c)/Re$ with $u_b(1)=0$. The first term of (20) reduces to Poiseuille flow as $m\to 0$ and the second to Womersley's solution [35]. The exact wall fluxes are $Nu=-\lambda I_1(\lambda)/I_0(\lambda)$ and $Sh=-\Phi I_1(\Phi)/I_0(\Phi)$.

Table 2 compares the numerical solution with Eqs. (19, 20). The velocity, temperature and concentration profiles agree with the exact solution to within 5×10^{-4} for all cases, which confirms the accuracy of the profiles shown in Section 4. The two-point wall gradients are first-order accurate and underestimate the exact magnitudes by about 2% for Nu, 2–4% for C_f and 4–7% for Sh; this bias is systematic and does not affect the trends reported in Table 3. The base case with $Ec=0.02$ differs from the $Ec=0$ case by less than 10^{-4} in u.

Table 2. *Verification against the exact solution ($Ec=0$, $N=41$, $\Delta t=0.01$): centreline velocity at peak forcing, maximum error over the velocity, temperature and concentration profiles, and wall quantities from the two-point difference compared with their exact values.*

Case	m^2	$u(0)$ numerical	$u(0)$ exact	Max. profile error	C_f numerical	C_f exact	Sh numerical	Sh exact
Base case	1	0.5760	0.5761	2.4×10^{-4}	1.6477	1.6958	−3.7370	−3.9333
$Ha=6$	9	0.3569	0.3570	2.4×10^{-4}	1.2528	1.3053	−3.7370	−3.9333
$Mo=8$	9	0.3569	0.3570	2.4×10^{-4}	1.2528	1.3053	−3.7370	−3.9333
$\alpha=90°$	4	0.4672	0.4673	2.4×10^{-4}	1.4609	1.5112	−3.7370	−3.9333
$Re=5$	1	0.8990	0.8992	1.5×10^{-4}	2.1639	2.2120	−2.5060	−2.5972
$Rd=2$	1	0.5641	0.5643	2.4×10^{-4}	1.6307	1.6790	−3.7370	−3.9333
$Sc=2$	1	0.5704	0.5705	4.3×10^{-4}	1.6337	1.6820	−5.3875	−5.8004

4. Results and Discussion

The parameters take the base values of Table 1, for which $m^2=1$. Each parameter of the model is varied in turn, and the resulting wall quantities are collected in Table 3.

4.1. Effect of the Magnetic Field and Cell Morphology on Velocity

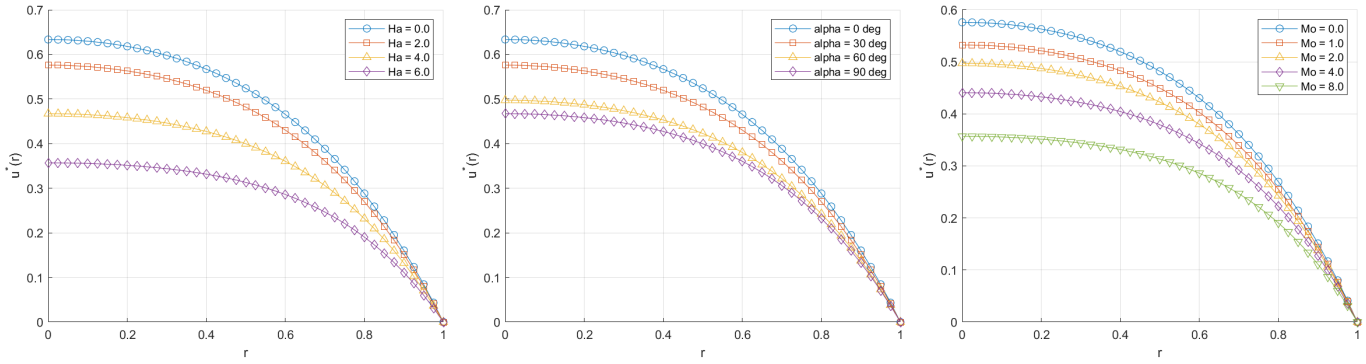
Figure 2 shows the velocity profiles for varying Hartmann number, field inclination and morphological parameter. All three retard the flow and flatten the core profile, because the

resistance m^2u/Re in Eq. (10) is largest where the velocity is largest. Increasing Ha from 0 to 6 lowers the centreline velocity from 0.634 to 0.357 (44%) as the stronger field induces larger currents and a stronger opposing Lorentz force; the skin friction falls from 1.738 to 1.253 (Table 3), in agreement with the trend reported for constant fields [26, 28].

The inclination of the field is an effective control variable in its own right Figure 2b). When the field is parallel to the flow ($\alpha = 0°$) it exerts no force and the velocity is highest; as α increases towards 90°, the transverse component $B_0 \sin\alpha$ grows and the centreline velocity falls from 0.634 to 0.467 (26%). The orientation of the field, and not only its magnitude, therefore determines the magnetic braking of the blood.

Figure 2c shows the morphological effect. As Mo increases from 0 (normal morphology) to 8 (severe sickling), the centreline velocity falls from 0.576 to 0.357 (38%) and the skin friction from 1.648 to 1.253 (24%). This reproduces, at the level of a single-phase continuum model, the increase in flow resistance and reduction in velocity caused by rigid sickle cells that cell-resolved simulations and clinical studies report [6, 8], and which underlies vaso-occlusion in narrow vessels.

The three panels also confirm the collapse onto m^2 (Eq. 16). The profile for $Ha = 6$ at $\alpha = 30°$ ($m^2 = 9$) coincides with that for $Mo = 8$ at $Ha = 2$ ($m^2 = 1 + 8$), both with centreline velocity 0.357, and Table 3 shows identical skin friction for $\alpha = 90°$ and $Ha = 4$ ($m^2 = 4$, $C_f = 1.4609$), for $\alpha = 60°$ and $Mo = 2$ ($m^2 = 3$, $C_f = 1.5145$), and for $\alpha = 0°$ and $Ha = 0$ ($m^2 = 0$, $C_f = 1.7384$). Magnetic and morphological resistance are therefore interchangeable, and the three parametric sweeps describe a single one-parameter family.



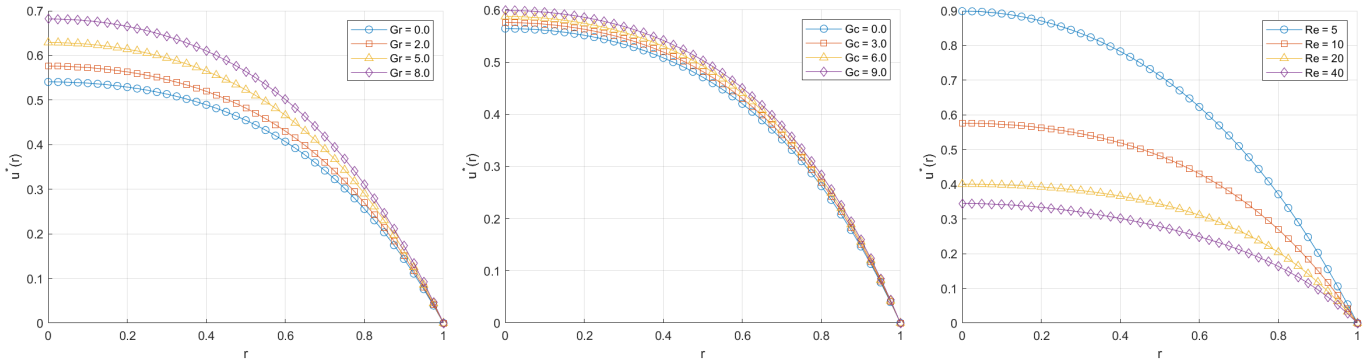
(a) (b) (c)

Figure 2. *Example of a cross-column figure with two subfigures.*

4.2. Effect of Buoyancy and Reynolds Number on Velocity

Increasing the thermal and solutal Grashof numbers accelerates the flow (Figure 3a, Figure 3b), since the buoyancy terms in Eq. (10) act as additional body forces aiding the pressure gradient. Raising Gr from 0 to 8 increases the centreline velocity from 0.541 to 0.682 and the skin friction from 1.569 to 1.883. The effect of Gc is weaker: raising Gc from 0 to 9 increases the centreline velocity only from 0.565 to 0.599. This is because the reacting species is confined to a thin layer near the wall ($c \approx 0.06$ on the axis in the base case), whereas the temperature remains close to the wall value across the whole section, so that thermal buoyancy acts on the core of the flow and solutal buoyancy mainly near the wall.

Increasing the Reynolds number (Figure 3c) reduces the dimensionless velocity, from 0.899 at $Re = 5$ to 0.345 at $Re = 40$, and lowers the skin friction from 2.164 to 1.093. In Eq. (10) the pressure forcing, the viscous term and the magnetic and morphological resistance all scale with $1/Re$, so that at higher Re the same pressure amplitudes produce a smaller velocity relative to U, and the profile becomes flatter because the oscillatory flow is increasingly dominated by inertia. The case $Re = 40$ is still slightly transient after four periods, since the decay rate of transients, $(j_{0,1}^2 + m^2)/Re$ with $j_{0,1} \approx 2.405$, decreases with Re; its wall values in Table 3 are marked accordingly.



(a) (b) (c)

Figure 3. *Velocity profiles at peak pressure forcing for varying (a) thermal Grashof number Gr, (b) solutal Grashof number Gc and (c) Reynolds number Re.*

4.3. Velocity over the Pulsatile Cycle

Figure 4 shows the centreline velocity over the fourth period of the pressure forcing for $Ha = 0$, 2 and 4. The magnetic field lowers both the mean and the extremes of the oscillation: the cycle-mean centreline velocity falls from 0.479 to 0.268 and the maximum from 0.885 to 0.590 as Ha increases from 0 to 4. At $Ha = 4$ the minimum becomes negative (-0.054), so that the centreline flow briefly reverses late in the cycle. The velocity peaks after the peak of the pressure forcing because of fluid inertia, and the field slightly reduces this phase lag: the extra resistance moves the flow from the inertia-dominated towards the quasi-steady, resistance-dominated regime. Because Ha, α and Mo act only through m^2, the same behaviour follows for increasing sickling, which therefore raises the relative amplitude of the oscillation and the likelihood of flow reversal near diastole.

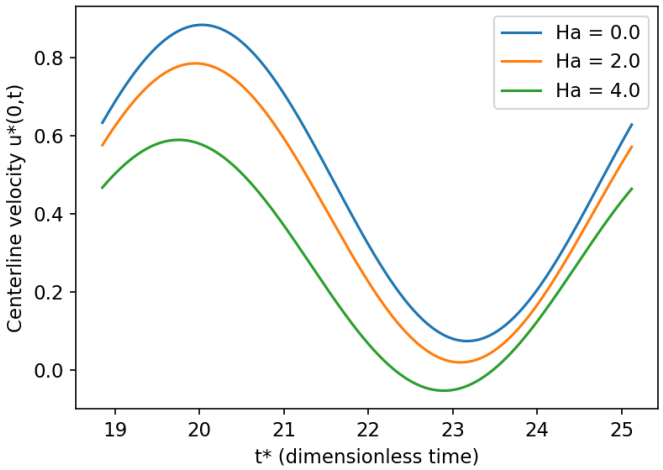
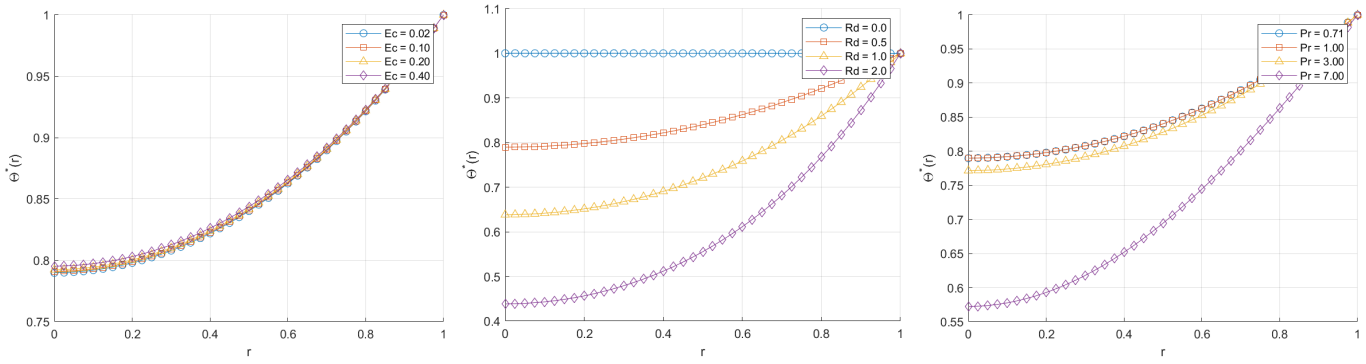


Figure 4. *Centreline velocity over one period of the pulsatile pressure forcing for varying Hartmann number Ha.*

4.4. Temperature Profiles

Figure 5a shows that increasing the Eckert number raises the temperature, since Ec scales the Joule and morphological heating in Eq. (11). The effect is small for the base resistance $m^2 = 1$: the centreline temperature rises from 0.790 to 0.796 as Ec increases from 0.02 to 0.4, and Nu changes from -0.439 to -0.433. The radiation parameter has a much stronger effect (Figure 5b). Without radiation ($Rd = 0$) the blood takes the wall temperature everywhere apart from the small dissipative heating, while increasing Rd to 2 lowers the centreline temperature to 0.439 and raises the magnitude of the wall heat flux from 0 to 1.363, because radiation acts as a volumetric heat sink that the wall must replenish. The computed profiles agree with the exact solution $\Theta = I_0(\lambda r)/I_0(\lambda)$ to within 10^{-4}.

Figure 5c shows the profiles at the end of the fourth period for increasing Prandtl number. Because the thermal relaxation rate $(j_{0,1}^2 + 2Rd)/(Re\,Pr)$ is inversely proportional to Pr, the temperature at higher Pr is still developing at this time: for $Pr = 7$ the core temperature is 0.573 rather than its periodic value of about 0.79, and the near-wall gradient is correspondingly steeper ($Nu = -0.715$). The figure therefore shows that heat penetrates from the wall into the blood more slowly as the momentum diffusivity grows relative to the thermal diffusivity, which produces a thinner thermal boundary layer during the transient. In the periodic state, the dependence of the temperature on Pr enters only through the small dissipative term and is weak.



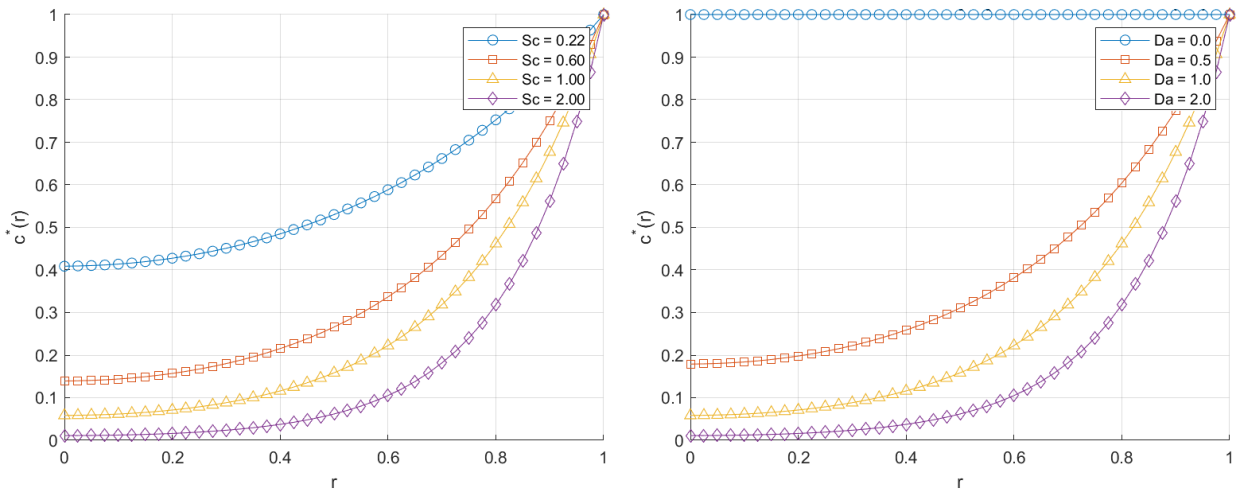
(a) (b) (c)

Figure 5. *Temperature profiles for varying (a) Eckert number Ec, (b) radiation parameter Rd and (c) Prandtl number Pr (at $t = 8\pi$; the profiles for $Pr = 3$ and 7 are still developing).*

4.5. Concentration Profiles

Figure 6 shows the concentration of the reacting species. Increasing the Schmidt number (Figure 6a) lowers the core concentration from 0.41 at $Sc = 0.22$ to 0.011 at $Sc = 2$, because a higher Sc means weaker molecular diffusion relative to momentum diffusion, so that the species released at the wall is consumed before it can diffuse to the axis. Increasing the Damköhler number (Figure 6b) has the same effect through faster chemical consumption. Without reaction ($Da = 0$) the concentration is uniform and equal to the wall value, while for $Da = 2$ the species is confined to a thin layer next to the wall. In both cases the concentration boundary layer becomes thinner and the magnitude of the Sherwood number increases (Table 3).

The periodic concentration depends only on the Thiele modulus $\Phi^2 = 2Re\,Sc\,Da$, and the Sherwood numbers in Table 3 confirm this exactly: $Re = 20$, $Sc = 2$ and $Da = 2$ all correspond to $\Phi^2 = 40$ and give $Sh = -5.3875$, and $Re = 5$ and $Da = 0.5$ both correspond to $\Phi^2 = 10$ and give $Sh = -2.5060$. The concentration is unaffected by the magnetic field, the morphology and buoyancy, because the flow is fully developed and the species is not advected radially. In SCA, haemolysis releases cell-free haemoglobin that scavenges nitric oxide produced by the endothelium [36, 37]; within the present framework this corresponds to a larger consumption rate and hence a larger Φ, which depletes the species in the core and steepens its near-wall gradient.



(a) (b)

Figure 6. *Concentration profiles for varying (a) Schmidt number Sc and (b) Damköhler number Da.*

4.6. Induced Magnetic Field

Because the flow is purely axial and independent of z, Eq. (13) has no source term. With zero initial and boundary data its solution is $b_r^* \equiv 0$ for all r, t and every value of Rm, which the numerical solution reproduces exactly. This is a direct consequence of the model assumptions rather than a numerical artefact, and it justifies the approximation $b_r \approx \sin\alpha$ in the momentum and energy equations. The axial induced field b_z, in contrast, is generated by the flow advecting the applied transverse field, through the source $\sin\alpha\, r^{-1}\partial_r(ru)$ in Eq. (14). Figure 7 shows that b_z is largest on the axis, vanishes at the wall and increases strongly with the magnetic Reynolds number: its centreline value rises from about 0.65 at $Rm = 1$ to about 10.2 at $Rm = 20$, since a larger Rm means weaker magnetic diffusion relative to advection. The induced field does not feed back on the flow in this model, so C_f, Nu and Sh are independent of Rm (Table 3).

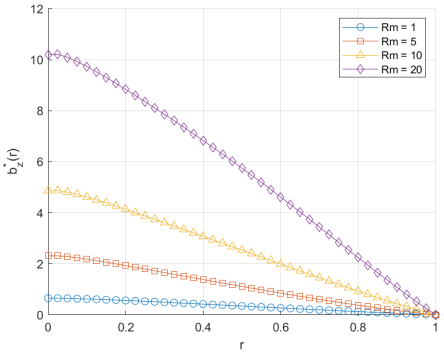


Figure 7. *Induced axial magnetic field b_z for varying magnetic Reynolds number Rm.*

4.7. Skin Friction, Nusselt and Sherwood Numbers

Table 3. *Skin friction C_f, Nusselt number Nu and Sherwood number Sh for every parametric sweep. Base values are marked with †; values marked ‡ are taken before the solution has fully reached its periodic state (see Sections 4.2 and 4.4).*

Parameter	Value	C_f	Nu	Sh	Parameter	Value	C_f	Nu	Sh
Ha	0	1.7384	−0.4395	−3.7370	Ec	0.02†	1.6477	−0.4392	−3.7370
Ha	2†	1.6477	−0.4392	−3.7370	Ec	0.1	1.6477	−0.4379	−3.7370
Ha	4	1.4609	−0.4386	−3.7370	Ec	0.2	1.6477	−0.4362	−3.7370
Ha	6	1.2528	−0.4381	−3.7370	Ec	0.4	1.6478	−0.4329	−3.7370
Gr	0	1.5691	−0.4392	−3.7370	Rd	0	1.6570	0.0004	−3.7370
Gr	2†	1.6477	−0.4392	−3.7370	Rd	0.5†	1.6477	−0.4392	−3.7370
Gr	5	1.7656	−0.4391	−3.7370	Rd	1	1.6406	−0.7970	−3.7370
Gr	8	1.8834	−0.4390	−3.7370	Rd	2	1.6307	−1.3630	−3.7370
Gc	0	1.5956	−0.4392	−3.7370	Pr	0.71†	1.6477	−0.4392	−3.7370
Gc	3†	1.6477	−0.4392	−3.7370	Pr	1	1.6477	−0.4391	−3.7370
Gc	6	1.6997	−0.4392	−3.7370	Pr	3‡	1.6466	−0.4623	−3.7370
Gc	9	1.7518	−0.4392	−3.7370	Pr	7‡	1.6382	−0.7147	−3.7370
Re	5	2.1639	−0.4384	−2.5060	Sc	0.22	1.6856	−0.4392	−1.4600
Re	10†	1.6477	−0.4392	−3.7370	Sc	0.6	1.6599	−0.4392	−2.7953
Re	20	1.3123	−0.4395	−5.3875	Sc	1†	1.6477	−0.4392	−3.7370
Re	40‡	1.0931	−0.4585	−7.5789	Sc	2	1.6337	−0.4392	−5.3875
Mo	0†	1.6477	−0.4392	−3.7370	Da	0	1.7274	−0.4391	0.0000
Mo	1	1.5755	−0.4390	−3.7370	Da	0.5	1.6645	−0.4392	−2.5060
Mo	2	1.5145	−0.4388	−3.7370	Da	1†	1.6477	−0.4392	−3.7370
Mo	4	1.4125	−0.4385	−3.7370	Da	2	1.6337	−0.4392	−5.3875
Mo	8	1.2528	−0.4381	−3.7370					
α	0°	1.7384	−0.4395	−3.7370	Rm	1	1.6477	−0.4392	−3.7370
α	30°†	1.6477	−0.4392	−3.7370	Rm	5†	1.6477	−0.4392	−3.7370
α	60°	1.5145	−0.4388	−3.7370	Rm	10	1.6477	−0.4392	−3.7370
α	90°	1.4609	−0.4386	−3.7370	Rm	20	1.6477	−0.4392	−3.7370

Table 3 gives the wall quantities (18) for every parametric sweep. The skin friction decreases monotonically with Ha, α and Mo, through magnetic and morphological damping of the wall shear, and with Re; it increases with Gr and Gc. The magnitude of the Nusselt number grows with Rd, because radiative cooling of the core steepens the wall temperature gradient, and decreases slightly with Ec, because internal heating flattens the near-wall gradient. The magnitude of the Sherwood number grows with Sc, Da and Re through the Thiele modulus, consistent with the thinner concentration boundary layers in Figure 6. The Rm sweep leaves all three quantities unchanged.

4.8. Physiological Relevance and Limitations

The parameter values of Table 1 follow earlier MHD studies of blood flow [26, 28] and are chosen to display the structure of the model clearly; several lie outside the physiological range. For blood, $\sigma \approx 0.7$ S m^{-1} [38] and $\mu \approx 3.5$ mPa s give $Ha = B_0 R\sqrt{\sigma/\mu} \approx 0.03$–$0.14$ in a middle cerebral artery ($R \approx 1.4$ mm) and 0.26–1.24 in the aorta ($R \approx 12.5$ mm) for clinical magnetic resonance imaging (MRI) fields of 1.5–7 T. The magnetic contribution $Ha^2 \sin^2\alpha$ to m^2 is therefore small in cerebral vessels compared with the morphological contribution, which is consistent with the small flow reductions predicted for the aorta at 10 T [20, 21] and the absence of clinically relevant haemodynamic changes in humans exposed to 8 T [39]. Values of Ha of order 2–6 correspond to larger vessels or stronger fields. Likewise, the magnetic Reynolds number of blood is $Rm = \mu_0 \sigma U R \sim 10^{-9}$, so the induced field is negligible *in vivo* [40], and the Rm sweep illustrates the structure of the induction equations rather than a physiological effect. The Prandtl number of blood is about 20–25, larger than the values used here.

Further limitations follow from the assumptions. The vessel is rigid, straight and uniform; blood is Newtonian, with sickling represented by a single uniform linear resistance Mo rather than by a two-phase or shear-thinning description; the electric field is neglected, which gives an upper bound on magnetic braking; viscous dissipation is omitted from the energy balance; and the model has not yet been calibrated against patient data. The verification of Section 3.2 shows that, within these assumptions, the computed profiles are accurate.

5. Conclusions

A mathematical model of pulsatile sickle cell blood flow in a cylindrical vessel under an inclined magnetic field, with morphological resistance, heat transfer, reactive mass transfer and magnetic induction, has been developed and solved with a Crank–Nicolson finite difference scheme. The main conclusions are as follows.

1) Increasing the Hartmann number or the morphological parameter retards the flow and lowers the skin friction: $Ha = 0 \to 6$ reduces the peak velocity by 44% and $Mo = 0 \to 8$ by 38%, quantifying how sickle cell morphology impedes blood flow.
2) The inclination of the magnetic field is an effective flow-control variable: rotating the field from parallel to perpendicular to the flow reduces the peak velocity by 26%.
3) The Hartmann number, field inclination and morphological parameter act only through $m^2 = Ha^2 \sin^2\alpha + Mo$, so magnetic and morphological resistance are interchangeable and a static field adds to, but cannot offset, the resistance due to sickling.
4) Over the pulsatile cycle, increasing resistance lowers the mean velocity more than its oscillation and can produce brief flow reversal.
5) Thermal and solutal buoyancy accelerate the flow; Joule and morphological heating raise the temperature slightly; thermal radiation cools the core and increases the wall heat flux; and higher Prandtl numbers slow the thermal development.
6) Higher Schmidt and Damköhler numbers deplete the species in the core and increase the wall mass flux, which depends only on the Thiele modulus $\Phi^2 = 2Re\,Sc\,Da$.
7) The radial induced field vanishes identically, while the axial induced field grows with the magnetic Reynolds number.
8) The numerical profiles agree with exact Bessel-function solutions to within 5×10^{-4}.

6. Recommendations

6.1. Recommendations for Further Studies

1) *Refined morphological model.* The single linear resistance Mo should be replaced or supplemented by a shape- and rigidity-dependent effective viscosity (Casson, power-law or micropolar models) or by a two-phase description that distinguishes sickled from normal cells, with oxygen-dependent sickling.
2) *Calibration and validation.* Mo and the other parameters should be calibrated from measured whole-blood viscosity of SCA patients, and the predicted velocities and wall shear stress compared with transcranial Doppler or phase-contrast MRI data [17, 18, 42].
3) *Vessel geometry.* The model should be extended to

stenosed, tapered, curved and bifurcating vessels and to compliant walls, since vaso-occlusion is associated with narrowed segments.

4) *Physiological parameters.* Computations with physiological values ($Pr \approx 21$, $Ha < 1.5$, $Rm \ll 1$) and with viscous dissipation included should be carried out, together with longer integration until all fields reach their periodic state.
5) *Complete electromagnetic modelling.* A three-dimensional MHD model including the induced electric field and realistic wall conductivity would give quantitative, rather than upper-bound, estimates of magnetic braking.
6) *Alternative numerical methods.* The model can be solved with spectral collocation or spectral relaxation methods for higher accuracy [41, 43–45], and the exact solutions given here can serve as benchmarks.

6.2. Recommendations for Policy and Practice

1) *Stroke screening.* Transcranial Doppler screening of children with SCA [42] should be expanded, particularly in sub-Saharan Africa where the burden is greatest [4].
2) *Disease-modifying therapy.* The model predicts that lowering the effective resistance of sickle cell blood restores flow and wall shear, which supports wider access to hydroxyurea and safe transfusion services.
3) *Magnetic resonance imaging.* Within this framework, the static fields of clinical scanners add little flow resistance in cerebral arteries compared with sickling, so the model gives no haemodynamic reason to restrict MRI in SCA patients; standard safety screening should continue.
4) *Research capacity.* Collaboration between mathematicians, engineers, haematologists and radiologists, and the creation of patient registries linking rheological and imaging data, would enable the calibration and validation recommended above.

Abbreviations

CFD	Computational Fluid Dynamics
MHD	Magnetohydrodynamics
MRI	Magnetic Resonance Imaging
RBC	Red Blood Cell
SCA	Sickle Cell Anaemia
SCD	Sickle Cell Disease

Acknowledgments

The authors thank the Department of Pure and Applied Mathematics, Jomo Kenyatta University of Agriculture and Technology, for supporting this work.

Author Contributions

Maurine Aloo: Conceptualization, Formal analysis, Methodology, Software, Validation, Visualization, Writing – original draft

Mathew Ngugi Kinyanjui: Conceptualization, Supervision

Edward Richard Onyango: Methodology, Supervision, Writing – review & editing

Data Availability Statement

All results can be reproduced from the model equations and parameters given in the paper. The MATLAB code of the Crank–Nicolson solver and the script that regenerates every figure and table entry are available from the corresponding author on reasonable request.

Conflicts of Interest

The authors declare no conflicts of interest.

References

[1] Pauling, L., Itano, H. A., Singer, S. J., Wells, I. C. (1949). Sickle cell anemia, a molecular disease. Science, 110(2865), 543-548. https://doi.org/10.1126/science.110.2865.543

[2] Kato, G. J., Piel, F. B., Reid, C. D., Gaston, M. H., Ohene-Frempong, K., Krishnamurti, L., et al. (2018). Sickle cell disease. Nature Reviews Disease Primers, 4, 18010. https://doi.org/10.1038/nrdp.2018.10

[3] Rees, D. C., Williams, T. N., Gladwin, M. T. (2010). Sickle-cell disease. The Lancet, 376(9757), 2018-2031.

[4] GBD 2021 Sickle Cell Disease Collaborators. (2023). Global, regional, and national prevalence and mortality burden of sickle cell disease, 2000-2021: a systematic analysis from the Global Burden of Disease Study 2021. The Lancet Haematology, 10(8), e585-e599. https://doi.org/10.1016/S2352-3026(23)00118-7

[5] Chien, S., Usami, S., Bertles, J. F. (1970). Abnormal rheology of oxygenated blood in sickle cell anemia. Journal of Clinical Investigation, 49(4), 623-634. https://doi.org/10.1172/JCI106273

[6] Connes, P., Renoux, C., Romana, M., Abkarian, M., Joly, P., Martin, C., et al. (2018). Blood rheological abnormalities in sickle cell anemia. Clinical Hemorheology and Microcirculation, 68(2-3), 165-172.

[7] Chaturvedi, P., Shah, S. R. (2023). Mathematical analysis for the flow of sickle red blood cells in microvessels for bio medical application. The Yale Journal of Biology and Medicine, 96(1), 13.

[8] Alizadeh, A., Dadvand, A. (2018). Effects of deformability of RBCs on their dynamics and blood flow passing through a stenosed microvessel: an immersed boundary-lattice Boltzmann approach. Theoretical and Computational Fluid Dynamics, 32, 91-107.

[9] Mattie, A. A., Alizadeh, A. (2019). Using a non-conforming meshes method to simulate an interaction between incompressible flow and rigid and elastic boundaries. Mechanics, 25(4), 276-282.

[10] Hassanzadeh, A., Pourmahmoud, N., Dadvand, A. (2017). Numerical simulation of motion and deformation of healthy and sick red blood cell through a constricted vessel using hybrid lattice Boltzmann-immersed boundary method. Computer Methods in Biomechanics and Biomedical Engineering, 20(7), 737-749.

[11] Shi, L., Pan, T.-W., Glowinski, R. (2012). Deformation of a single red blood cell in bounded Poiseuille flows. Physical Review E, 85(1), 016307.

[12] Ye, T., Li, H., Lam, K. Y. (2010). Modeling and simulation of microfluid effects on deformation behavior of a red blood cell in a capillary. Microvascular Research, 80(3), 453-463.

[13] Ye, T., Phan-Thien, N., Lim, C. T., Li, Y. (2017). Red blood cell motion and deformation in a curved microvessel. Journal of Biomechanics, 65, 12-22.

[14] Ye, T., Peng, L. (2019). Motion, deformation, and aggregation of multiple red blood cells in three-dimensional microvessel bifurcations. Physics of Fluids, 31(2).

[15] Freund, J. B. (2014). Numerical simulation of flowing blood cells. Annual Review of Fluid Mechanics, 46, 67-95.

[16] Kotsalos, C., Latt, J., Chopard, B. (2019). Bridging the computational gap between mesoscopic and continuum modeling of red blood cells for fully resolved blood flow. Journal of Computational Physics, 398, 108905.

[17] Keller, S. B., Bumpus, J. M., Gatenby, J. C., Yang, E., Kassim, A. A., Dampier, C., et al. (2021). Characterizing intracranial hemodynamics in sickle cell anemia: impact of patient-specific viscosity. Cardiovascular Engineering and Technology, 1-16.

[18] Sawyer, R. P., Pun, S., Karkoska, K. A., Clendinen, C. A., DeBaun, M. R., Gutmark, E., et al. (2022). Effect of blood transfusion on cerebral hemodynamics and vascular topology described by computational fluid dynamics in sickle cell disease patients. Brain Sciences, 12(10), 1402.

[19] Tekleab, Y., Harris, W. (2012). A two-dimensional model of blood plasma flow with oxygen transport and blood cell membrane deformation. Seventh International Conference on Computational Fluid Dynamics (ICCFD7), Paper ICCFD7-3205.

[20] Tenforde, T. S. (2005). Magnetically induced electric fields and currents in the circulatory system. Progress in Biophysics and Molecular Biology, 87(2-3), 279-288.

[21] Kinouchi, Y., Yamaguchi, H., Tenforde, T. S. (1996). Theoretical analysis of magnetic field interactions with aortic blood flow. Bioelectromagnetics, 17(1), 21-32.

[22] Tzirtzilakis, E. E. (2005). A mathematical model for blood flow in magnetic field. Physics of Fluids, 17(7), 077103.

[23] Atalla, A., Nagarkar, K., Ashe, J. (2014). Modeling the magnetic disturbance of pulsatile blood flow in a static magnetic field. In: 36th Annual International Conference of the IEEE Engineering in Medicine and Biology Society, 1406-1409.

[24] Prakash, J., Makinde, O. D. (2011). Radiative heat transfer to blood flow through a stenotic artery in the presence of magnetic field. Latin American Applied Research, 41(3), 273-277.

[25] Chinyoka, T., Makinde, O. D. (2014). Computational dynamics of arterial blood flow in the presence of magnetic field and thermal radiation therapy. Advances in Mathematical Physics, 2014, 915640. https://doi.org/10.1155/2014/915640

[26] Sankar, A., Gunakala, S. R., Comissiong, D. (2014). The effect of heat transfer on two-layered blood flow through a composite stenosis in the presence of a magnetic field. International Journal of Applied Mathematics and Statistical Sciences, 3, 17-28.

[27] Sankar, A. R., Gunakala, S. R., Comissiong, D. M. G. (2022). Finite element analysis of oxygen transfer from blood in permeable microcirculation to surrounding tissue in the presence of a magnetic field. Palestine Journal of Mathematics, 11.

[28] Ekakitie, O., Isaac, F., Osinowo, O., Izah, S. C., Dauseye, K. E., Kubugha, B. W. (2023). Mathematical modelling for improved blood flow in a sickle cell anaemia patient with morphological effect. American Journal of Applied Mathematics, 11(3), 40-51.

[29] Thess, A., Votyakov, E., Knaepen, B., Zikanov, O. (2007). Theory of the Lorentz force flowmeter. New Journal of Physics, 9(8), 299.

[30] Nield, D. A., Bejan, A. (2017). Convection in Porous Media (5th ed.). Cham: Springer.

[31] Cogley, A. C., Vincenti, W. G., Gilles, S. E. (1968). Differential approximation for radiative transfer in a nongray gas near equilibrium. AIAA Journal, 6(3), 551-553.

[32] Crank, J., Nicolson, P. (1947). A practical method for numerical evaluation of solutions of partial differential equations of the heat-conduction type. Mathematical Proceedings of the Cambridge Philosophical Society, 43(1), 50-67.

[33] Morton, K. W., Mayers, D. F. (2005). Numerical Solution of Partial Differential Equations (2nd ed.). Cambridge: Cambridge University Press.

[34] Abramowitz, M., Stegun, I. A. (1964). Handbook of Mathematical Functions with Formulas, Graphs, and Mathematical Tables. Washington, DC: National Bureau of Standards.

[35] Womersley, J. R. (1955). Method for the calculation of velocity, rate of flow and viscous drag in arteries when the pressure gradient is known. Journal of Physiology, 127(3), 553-563.

[36] Reiter, C. D., Wang, X., Tanus-Santos, J. E., Hogg, N., Cannon, R. O., Schechter, A. N., et al. (2002). Cell-free hemoglobin limits nitric oxide bioavailability in sickle-cell disease. Nature Medicine, 8(12), 1383-1389.

[37] Kato, G. J., Gladwin, M. T., Steinberg, M. H. (2007). Deconstructing sickle cell disease: reappraisal of the role of hemolysis in the development of clinical subphenotypes. Blood Reviews, 21(1), 37-47.

[38] Gabriel, S., Lau, R. W., Gabriel, C. (1996). The dielectric properties of biological tissues: III. Parametric models for the dielectric spectrum of tissues. Physics in Medicine and Biology, 41(11), 2271-2293.

[39] Chakeres, D. W., Kangarlu, A., Boudoulas, H., Young, D. C. (2003). Effect of static magnetic field exposure of up to 8 Tesla on sequential human vital sign measurements. Journal of Magnetic Resonance Imaging, 18(3), 346-352.

[40] Davidson, P. A. (2001). An Introduction to Magnetohydrodynamics. Cambridge: Cambridge University Press.

[41] Chepkonga, D. K., & Ndede, C. O. (2026). Toward electromagnetically tunable solar-thermal receivers: Induced-field (EMHD) dynamics of a Cu–TiO2/water hybrid nanofluid in a parabolic collector. Results in Physics, 108759.

[42] Adams, R. J., McKie, V. C., Hsu, L., Files, B., Vichinsky, E., Pegelow, C., et al. (1998). Prevention of a first stroke by transfusions in children with sickle cell anemia and abnormal results on transcranial Doppler ultrasonography. New England Journal of Medicine, 339(1), 5-11.

[43] Chepkonga, D. K. (2026). Spectral relaxation analysis of rotating magnetohydrodynamic viscous flow and heat transfer past a stretching sheet. Results in Engineering, 110985.

[44] Chepkonga, D., Kinyanjui, M., Kiogora, R., Giterere, K. E. (2025). Modelling heat and mass transfer in gyro-tactic hybrid nanofluid flow through a converging pipe with injection and suction. International Journal of Ambient Energy, 46(1), 2442592.

[45] Chepkonga, D., Kinyanjui, M., Kiogora, R., Giterere, K. E. (2025). Numerical study of multiphase hybrid gyrotactic nanofluid flow through porous convergent pipe with injection and suction. Engineering Letters, 33(2), 357-373.